Electronic Supplementary Information for:

Observing long-range non-fullerene backbone ordering in real-space to improve charge transport properties of organic solar cells

Zhaozhao Bi,[a] Kai Chen,[bc] Lu Gou,[d] Yuan Guo,[eg] Xiaobo Zhou,[a] Hafiz Bilal Naveed,[a] Jing Wang,[f] Qinglian Zhu,[a] Jian Yuan,[a] Chao Zhao,[a] Ke Zhou,[a] Sreelakshmi Chandrabose,[c] Zheng Tang,[f] Yuanping Yi,[e] Justin M. Hodgkiss*[c], Lei Zhang,*[d], Wei Ma*[a]

[a] State Key Laboratory for Mechanical Behavior of Materials, Xi'an Jiaotong University, Xi'an 710049, China. E-mail: msewma@xjtu.edu.cn.

[b] Robinson Research Institute, Victoria University of Wellington, Lower Hutt 5046, New Zealand and MacDiarmid Institute for Advanced Materials and Nanotechnology, New Zealand.

[c] MacDiarmid Institute for Advanced Materials and Nanotechnology, and School of Chemical and Physical Sciences, Victoria University of Wellington, Wellington 6010, New Zealand. E-mail: justin.hodgkiss@vuw.ac.nz

[d] MOE Key Laboratory for Nonequilibrium Synthesis and Modulation of Condensed Matter, School of Physics, Xi'an Jiaotong University, Xi'an 710049, China. E-mail: zhangleio@mail.xjtu.edu.cn.

[e] Beijing National Laboratory for Molecular Science, Key Laboratory of Organic Solids, Institute of Chemistry, Chinese Academy of Sciences, 100190 Beijing, China

[f] Center for Advanced Low-dimension Materials, State Key Laboratory for Modification of Chemical Fibers and Polymer Materials, College of Materials Science and Engineering, Donghua University, Shanghai 201620, China.

[g] School of Light Industry and Engineering, Qilu University of Technology (Shandong Academy of Sciences), Jinan 250353, China

Content

1. Measurements and Characterizations

Materials: PM6 (Solarmer Materials Inc.), Y6 (eFlexPV Inc.), and $PC_{71}BM$ (Solenne BV Inc.) were used as received without further purification.

Device fabrication and characterization: Conventional structure of ITO/PEDOT:PSS/Active layer/PFN-Br/Al was utilized to evaluate the device performance. The ITO-coated substrates were sequentially cleaned by ultrasonication in detergent-water mixture, deionized water, acetone, and isopropanol (each step for 30 min). The cleaned glass substrates were further exposure by oxygen plasma for 20 min. PEDOT:PSS (Heraeus Clevios PVP AI 4083) was spin-coated on the prepared ITO glasses with a thickness of about 30 nm and baked at 150 ^{o}C for 15 min in air. Then the glasses were transferred to a nitrogen glove box, where the solutions with donors and acceptors were spun onto the PEDOT:PSS surface to get 110 nm thick films via varied spin-coating rates. The solution was prepared in chloroform with 0.5% 1-chloronaphthalen, stirred overnight on a 30 ^{o}C hotplate. Solvent vapor annealing was conducted by the inverted solvent annealing of CS_2 about 10 seconds in customized evaporating dish. Afterwards, a thin PFN-Br layer (1 mg/mL in methanol, 3000 rpm for 30 s, about 15 nm) was spin coated on the active layer. Finally, 100 nm Al were deposited at a vacuum level of $< 1\times10^{-4}$ Pa. Typical devices area (0.04 cm^2) was defined by a metal mask with aligned aperture. The *J-V* characteristics were carried out using an AAA solar simulator (SS-F5-3A, Enlitech) in glove box. The radiative intensity (AM 1.5G spectrum, 100 mW cm^{-2}) was calibrated by a standard silicon cell with a KG5 filter (calibrated by Enli Tech. Optoelectronic Calibration Lab.) and a Keighley 2400 source meter unit. *J-V* curves were measured in the forward direction from -0.5 to 1.0 V, with a scan step of 20 mV and a dwell time of 1 ms. The EQE data were collected using the integrated spectral response system (QE-R3018, Enlitech).

Cryo-EM: The Cryo-EM samples were floated on a glow-discharged holey carbon film-coated copper grid (QUANTIFOIL® R 2/2, Electron Microscopy Sciences). Grids were blotted manually using a custom-built manual plunger at room temperature. Samples were blotted for 4-5 s with Whatman No.1 filter paper immediately before plunge freezing in liquid ethane cooled by liquid nitrogen. The flash-frozen grids were transferred into liquid nitrogen for storage. Cryo-EM samples were examined using a FEI Talos F200C TEM operating at 200 KV high tension at -178 ^{o}C in low dose mode. A Gatan 626 cryo-holder was used. The

micrographs were acquired with a high-sensitivity 4K×4K pixel FEI CETA CMOS camera under the magnifications of 13500×-120k×. TEM images were obtained using the same microscope.

Molecular dynamics simulations: The geometric structures of Y6 and $PC_{61}BM$ are optimized by density functional theory (DFT) at the B3LYP/6-31G(d,p) level. To gain an insight into the intermolecular packing of Y6 and $PC_{61}BM$, the thin films were built and imitated by atomistic molecular dynamic simulations with the Gromacs-4.6.7 software package. The films were simulated by the following procedure: (i) solutions were constructed to contain 400 Y6 molecules or 400 Y6:166 $PC_{61}BM$ molecules along with 50000 chloroform (CF) solvent molecules; then NPT equilibration was performed at 300 K and 100 bar for 2 ns to make molecules close together quickly (compression) and then at 300K and 1bar for 20 ns. (ii) a quasi-equilibrium approach was exploited to imitate solvent evaporation processes by randomly removing 100 solvent molecules every 100 ps from the solutions. (iii) After removing all solvent molecules, the dried samples were further equilibrated for 30 ns.

Transient absorption spectroscopy. We used transient absorption (TA) to study the materials' excitation dynamics in the time scales from sub-picosecond to 3 nanoseconds. The basic TA setup is described in previous literature.[1,2] A 3 kHz, 100 fs, An 1 mJ Ti-sapphire amplifier (Spitfire by Spectral-physics) is the light source to generate the pump beam by an optical parametric amplifier (TOPAS) and probe beam by supercontinuum generation from an undoped YAG crystal. A motorized optical delay line controls the time delay between the pump and probe beams. An optical chopper, trigged by the laser and operated at 1.5 kHz, modulates the pump beam. The pump and probe beams were focused and overlapped on the sample. After passing the sample, the visible and NIR parts of the broadband probe were sent to a visible and NIR spectrometer, respectively. Two synchronized cameras collect the visible (450 – 1000 nm) and NIR (800 – 1600 nm) spectral regions of the probe continuum. To detect TA signals, we employ shot-to-shot detection scheme by measuring the spectrum of each probe pulse with and without sample excitation. Three thousand shot pairs were averaged for each TA spectral at a time delay point. All the samples are measured dynamic vacuum environment to avoid photodegradation.

GIWAXS characterization: GIWAXS measurements were performed at beamline 7.3.3[3] at the Advanced Light Source. Samples were prepared on Si substrates using identical blend

solutions as those used in devices. The 10 keV X-ray beam was incident at a grazing angle of 0.11°-0.15°, selected to maximize the scattering intensity from the samples. The scattered x-rays were detected using a Dectris Pilatus 2M photon counting detector.

RSoXS characterization: RSoXS transmission measurements were performed at beamline 11.0.1.2[4] at the Advanced Light Source (ALS). Samples for R-SoXS measurements were prepared on a PSS modified Si substrate under the same conditions as those used for device fabrication, and then transferred by floating in water to a 1.5 mm × 1.5 mm, 100 nm thick Si3N4 membrane supported by a 5 mm × 5 mm, 200 μm thick Si frame (Norcada Inc.). 2-D scattering patterns were collected on an in-vacuum CCD camera (Princeton Instrument PI-MTE). The sample detector distance was calibrated from diffraction peaks of a triblock copolymer poly(isoprene-b-styrene-b-2-vinyl pyridine), which has a known spacing of 391 Å. The beam size at the sample is approximately 100 μm by 200 μm.

Hole and electron mobility measurement: Hole-only devices were fabricated using the architectures of ITO/PEDOT:PSS/Active layer/MoO_x/Al. Electron-only devices were fabricated using the structures of ITO/ZnO/Active layer/PFN-Br/Al. The mobilities were calculated using space charge limited current (SCLC) model by fitting the current density-voltage curves and calculated by the equation:[5,6]

$$J = 9\varepsilon_0\varepsilon_r\mu(V_{appl} - V_{bi} - V_s)^2/8L^3$$

Where J is current density, ε_0 is the permittivity of free space, ε_r is the relative permittivity of the material (assumed to 3), μ is hole mobility or electron mobility, V_{appl} is applied voltage, V_{bi} is the built-in voltage, V_s is the voltage drop from the substrate's series resistance (V_s=IR) and L is the thickness of film.

Transient photovoltage measurement: The lifetime of carriers can be measured by the transient photovoltage measurement. The background illumination was provided by a normal LED light source, and pulsed light was provided by arbitrary wave generator (AFG322C, Tektronix). The photovoltage traces were registered by the oscilloscope (AFG322C, Tektronix).

2. Molecular packing in Y6 thin films

2.1 GIWAXS analysis

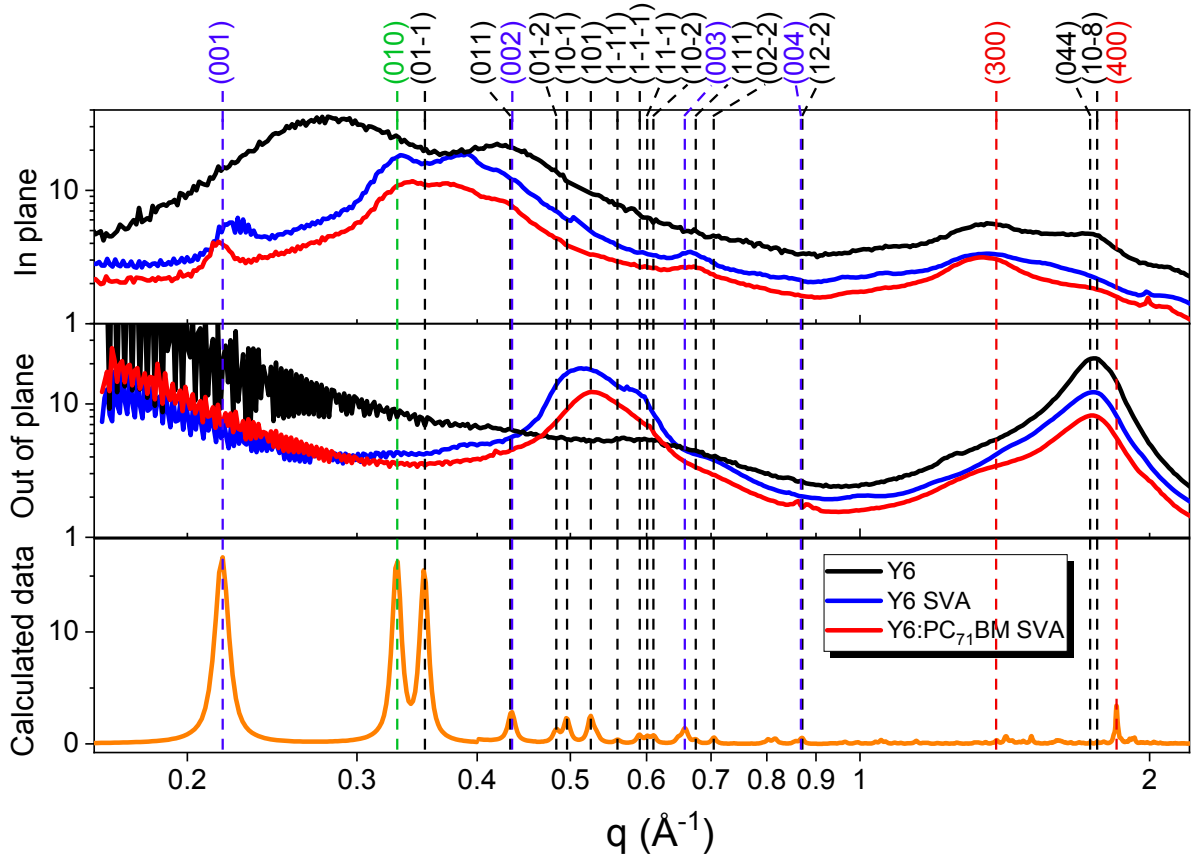

Figure S1. The GIWAXS line curves and calculated scattering peaks.

Note S1.

The GIWAXS line curves correspong to the 2D patterns shown in Figure 1b. The calculated data was simulated using the Mercury software 3.8 (Build RC2) based on the Y6 sing crystall data released by Cao et al.[7] The GIWAXS diffraction curves are labeled with the (*hkl*) miller indices on repesctive peaks. According to the calculated results, the red labels indicate the crystal planes parallel to the *bc* plane of unit cell and suggest the ordered Y6 packing perpendicular to the backbone plane. The green labels indicate the lattice planes parallel to the ca plane of unit cell. The blue labels indicate the crystal planes parallel to the ab plane of unit cell. Due to the unique banana-like shape and the end-group and core linked stacking of Y6, we can refer the green and blue planes as the presence of Y6 backbone packing along the b- and c-axis, respectively (illustrated in Figure 1c). According to Figure S1, we can always assign the scattering peaks to the corresponding lattice planes based on the simulation results, except for the peak at about 0.3 $Å^{-1}$. We consider this suggests two

important things. On the one hand, the Y6 single-crystal data and the simulation results are reliable. On the other hand, the mismatch between simulation and GIWAXS characterization at 0.3 $Å^{-1}$ indicates that the scattering peak may not come from within individual unit cell, but is caused by the packing structure among the multi-crystals. Considering this peak is only prominent in the weakly crystalline neat Y6 film, it is reasonable to assign this scattering peak to the packing among the micro grains.

After understanding the above assignment, we are able to say the packing structures of Y6 has obviously changed in Y6 SVA and Y6:PC_{71}BM SVA films. Importantly, the presence of (001) peak in Y6 SVA and Y6:PC_{71}BM SVA films indicates the improved backbone packing of Y6 molecules along the IP direction. We note that the (002), (003), and even (010) peaks exhibit lower validity than (001) peak in calculating the coherence length of backbone packing, which mainly suffer from the overlapped signal of lattic planes. Nevertheless, the overall Y6 crystallinity can be evaluated by fitting these peaks due to its insensitivity to specific packing structure.

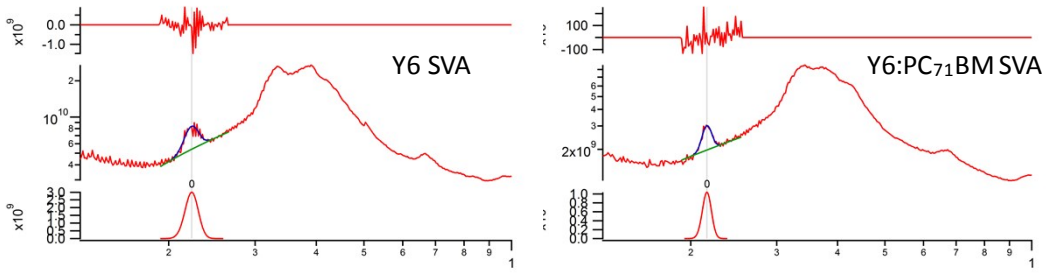

	Type	Location/$Å^{-1}$	FWHM/$Å^{-1}$	d-spacing/nm	coherence length/nm
Y6 SVA	Gauss	0.22	0.02	2.82	34.7
Y6:PC_{71}BM SVA	Gauss	0.22	0.01	2.91	52.2

Figure S2. The Gaussian fit of (001) peak in Y6 SVA and Y6:PC_{71}BM SVA films.

2.1 Molecular dynamics (MD) simulations

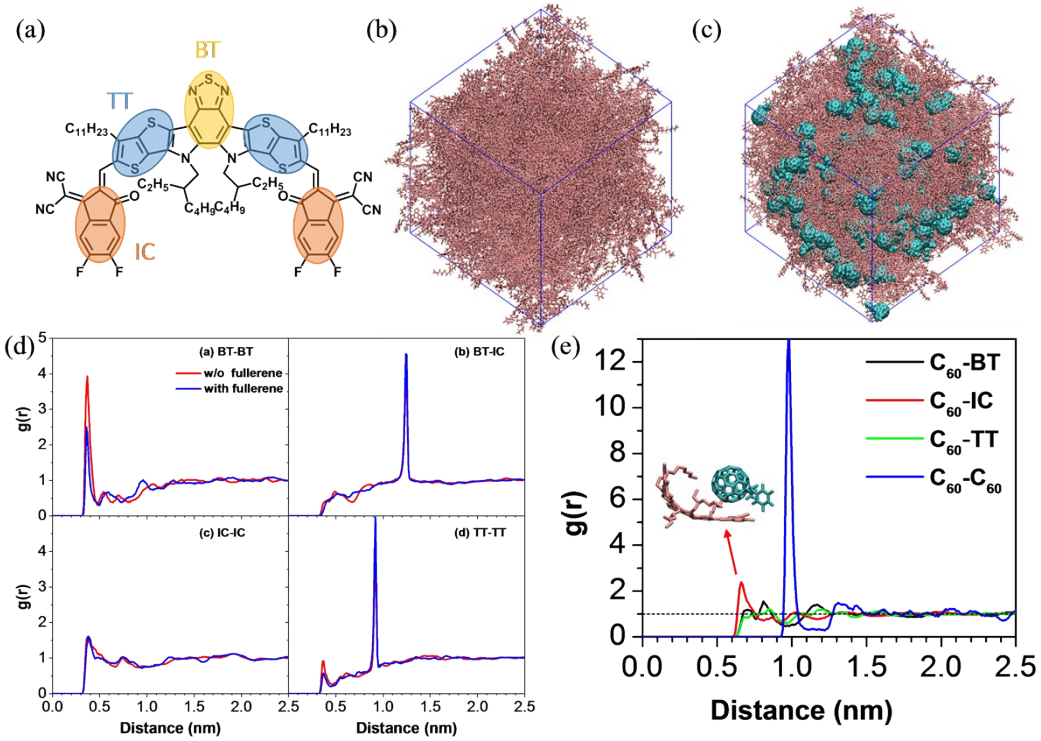

Figure S3. (a) Chemical structure of Y6. (b-c) Unit cell of equilibrated systems with Y6 and Y6:fullerene. (d) Center-of-mass redial distribution functions (RDFs) of Y6 that with or without fullerene. (e) Center-of-mass RDFs of system with fullerene. RDFs is the probability of finding other particles near around by drawing a series of circles about one certain particle.

3. Molecular packing in PM6:Y6 blend films

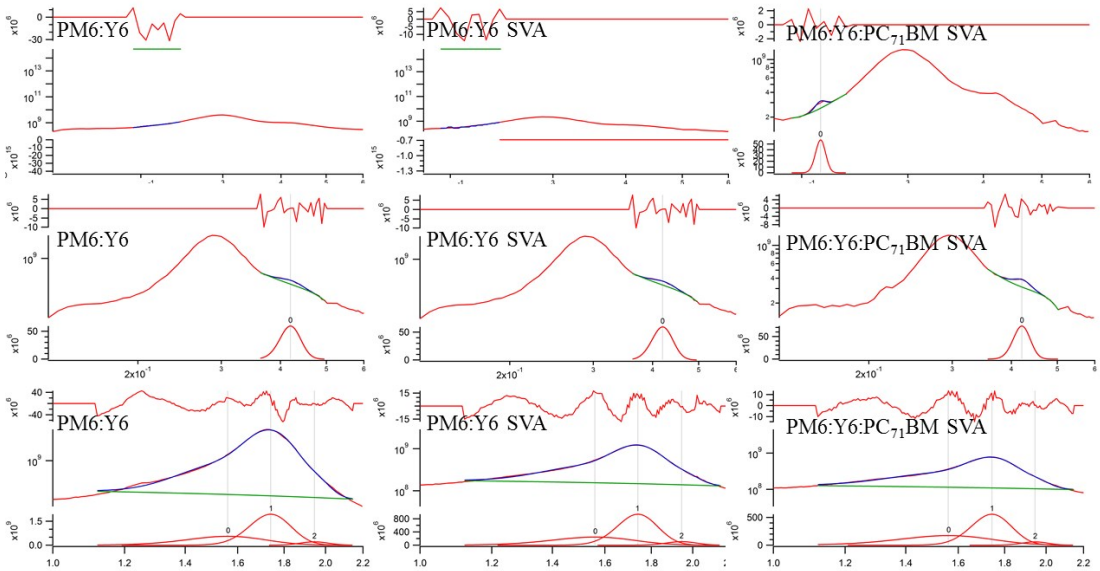

	OoP				IP			
	Location/Å^{-1}	FWHM/Å^{-1}	d-spacing/Å	L_A/Å	Location/Å^{-1}	FWHM/Å^{-1}	d-spacing/nm	L_A/nm
PM6:Y6	1.56	0.37	4.0	15.5	--			
	1.74	**0.22**	**3.6**	**26.1**	**0.43**	**0.05**	**1.47**	**10.3**
	1.95	0.16	3.2	34.6				
PM6:Y6 SVA	1.56	0.36	4.0	15.5	--	--	--	--
	1.74	**0.21**	**3.6**	**27.2**	**0.42**	**0.05**	**1.49**	**11.3**
	1.94	0.18	3.2	32.1				
	1.56	0.36	4.0	15.5	**0.21**	**0.01**	**2.92**	**58.6**
PM6Y6PC$_{71}$BM SVA	**1.74**	**0.18**	**3.6**	**30.9**	**0.42**	**0.04**	**1.49**	**13.8**
	1.94	0.20	3.2	28.9				

Figure S4. The Gaussian fit of (001), (002) and π-π in PM6:Y6, PM6:Y6 SVA, and PM6:Y6:PC$_{71}$BM SVA films, respectively.

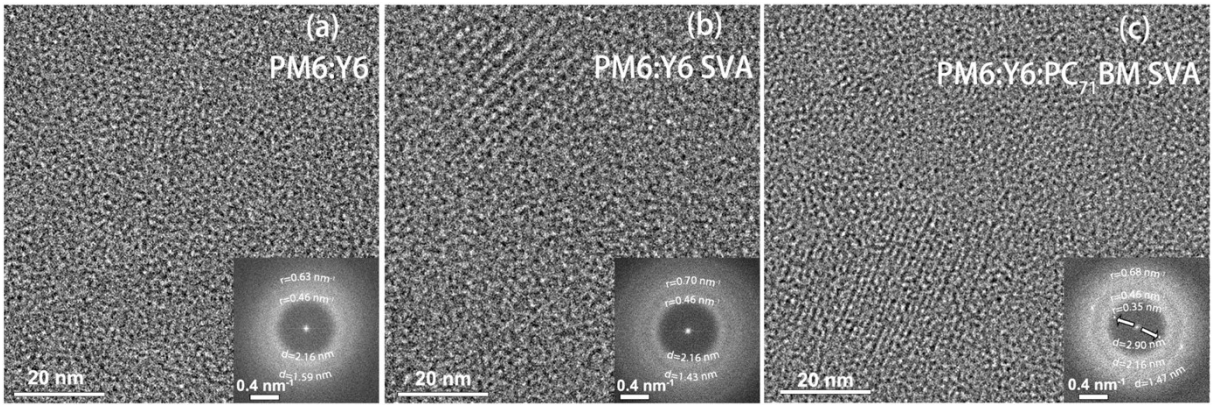

Figure S5. (a-c) Cryo-TEM images of PM6:Y6, PM6:Y6 SVA, and PM6:Y6:PC$_{71}$BM SVA films. The insert images were processed using fast fourier transform (FFT). The white arrows highlight two FFT points corresponding to the (001) scattering peak.

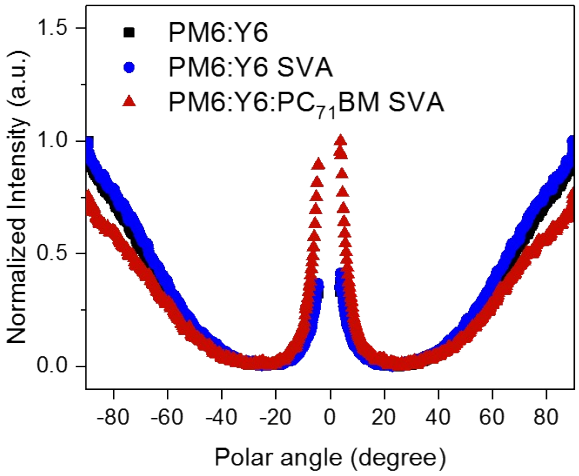

Figure S6. Background corrected and normalized integrated peak at ~0.3 $Å^{-1}$ as a function of polar angle.

4. Phase separation in PM6:Y6 blend films

4.1 TEM of PM6:Y6 blends

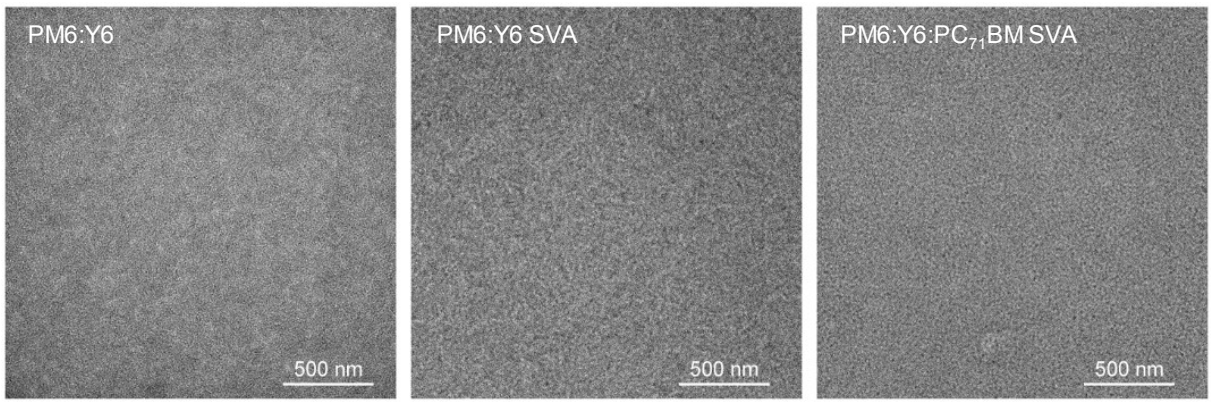

Figure S7. Bright-field TEM images of PM6:Y6, PM6:Y6 SVA, and PM6:Y6:PC_{71}BM SVA films.

4.2 Material contrast of PM6, Y6, and PCBM

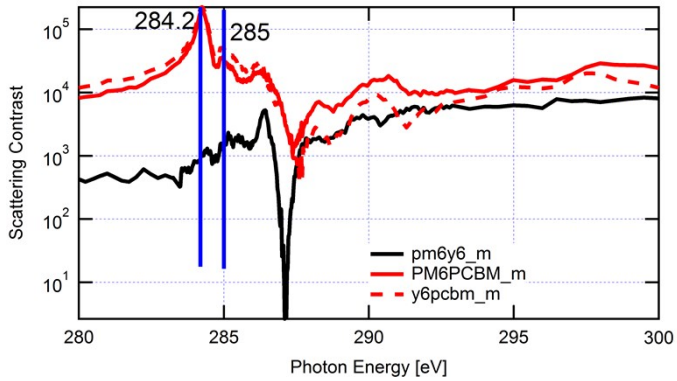

Figure S8. Scattering contrasts calculated between different components.

4.3 RSoXS of PM6:Y6 blends

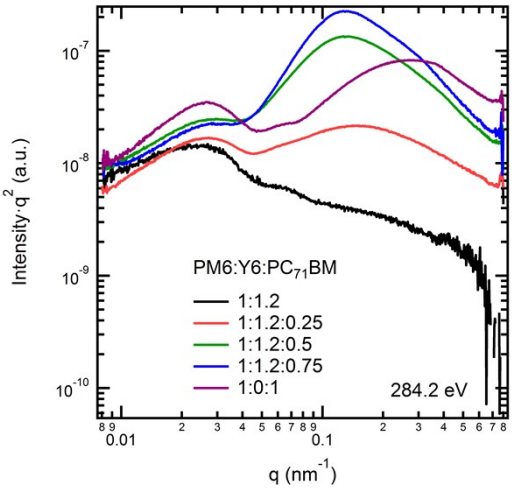

PM6:Y6:$PC_{71}BM$	Domain Size (nm)
1:1.2	18.6
1:1.2:0.25	20.5
1:1.2:0.5	23.8 & 10.3
1:1.2:0.75	24.4 & 11.3
1:0:1	11.9

Figure S9. The RSoXS scattering profiles and domain size at 284.2 eV for various $PC_{71}BM$ ratio blends.

5. PCBM ratio modification in ternary devices

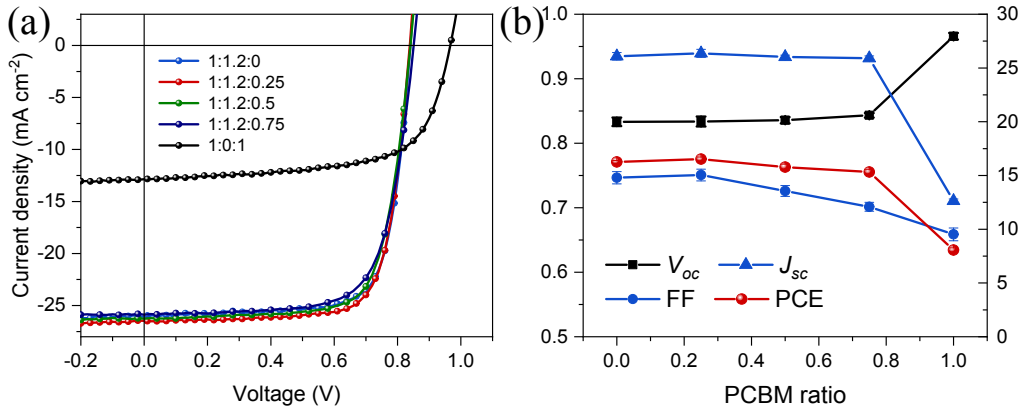

Figure S10. (a) J-V curves, and (b) Devices parameter function with $PC_{71}BM$ ratio in ternary devices.

Table S1. Detailed photovoltaic parameters of the ternary devices with SVA processing under AM 1.5G 100 mW cm^{-2} illumination.

t-OSC [a),b)]	V_{oc} (V)	J_{sc} (mA/cm^2)	FF (%)	Efficiency (%)
PM6:Y6 SVA	0.833±0.007	26.09±0.35	74.65±0.95	16.26±0.14 (16.56)
0.25 $PC_{71}BM$ SVA	0.834±0.008	26.36±0.37	75.07±0.91	16.53±0.19 (16.82)
0.5 $PC_{71}BM$ SVA	0.836±0.005	26.02±0.17	72.59±0.84	15.78±0.27 (16.25)
0.75 $PC_{71}BM$ SVA	0.843±0.004	25.91±0.22	70.15±0.69	15.32±0.22 (15.66)
PM6:$PC_{71}BM$ SVA	0.966±0.005	12.64±0.18	65.88±0.99	8.06±0.2 (8.59)

a) Average values with standard deviation were obtained from at least 20 independent devices.

b) The values in the brackets are the parameters of the best device.

6. Voltage losses analysis

Due to PM6:Y6:$PC_{71}BM$ SVA device shows red-shifted absorption and EQE edges, but exhibits similar V_{oc} value to PM6:Y6 SVA device. We studied the voltage losses (V_{loss}) to figure out the reasons. We divided the voltage losses into two parts: charge generation loss (E_g - E_{CT}) and charge recombination loss (E_{CT} - qV_{oc}). We first derived the bandgap (E_g) from the differential of device EQE. As shown in Figure S11, PM6:Y6 SVA and PM6:Y6:$PC_{71}BM$ SVA devices show gradually reduced bandgap. The energy of charge-transfer state (E_{CT}) is determined by electroluminescence (EL) and s-EQE spectra referred from Marcus theory

(Figure S12). As summarized in Table S2, the varied E_g and E_{CT} yields raised charge generation loss of 0.11 eV with SVA and $PC_{71}BM$ treatment, suggesting higher driving energy towards efficient exciton dissociation. On the other hand, the charge recombination loss is gradually reduced and finally filling up the increase of charge generation loss and resulting in decreased V_{loss} for PM6:Y6:$PC_{71}BM$ SVA device. To conclude, for the SVA processed device, V_{loss} remains similar, hence reducing the bandgap can decrease the V_{oc}. For SVA and $PC_{71}BM$ processed device, the decreased V_{loss} is responsible for the similar V_{oc}, even with the reduced bandgap.

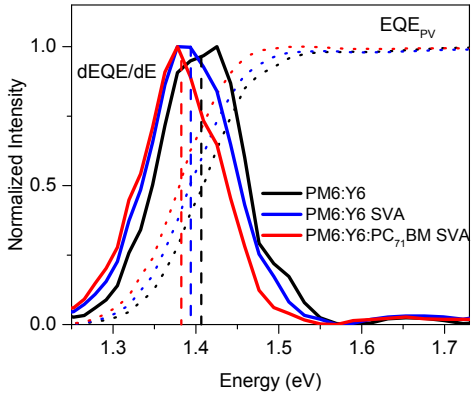

Figure S11. The determination of device bandgaps.

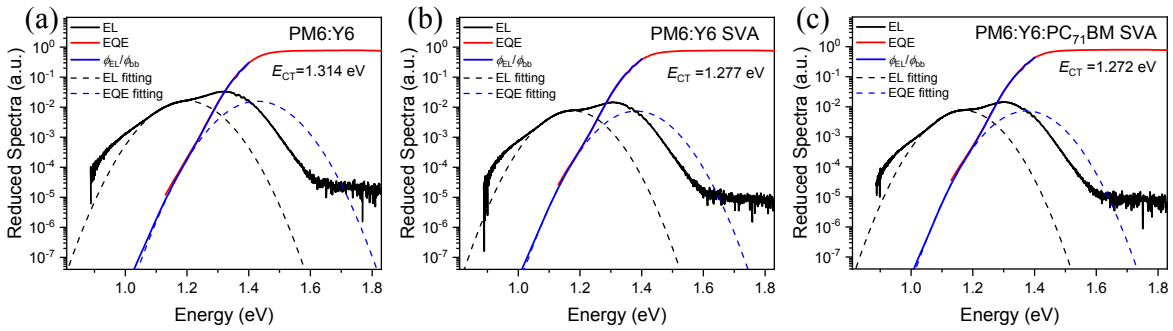

Figure S12. The reduced spectra of EL and s-EQE for the estimation of E_{CT}.

Table S2. Analysis of voltage losses for the devices.

	V_{loss}	E_g	qV_{oc}	E_{CT}	E_g-E_{CT}	E_{CT}-qV_{oc}
PM6:Y6	0.56	1.41	0.847	1.31	0.10	0.46
PM6:Y6 SVA	0.56	1.39	0.833	1.28	0.11	0.45
PM6:Y6:$PC_{71}BM$ SVA	0.55	1.38	0.834	1.27	0.11	0.44

7. Carrier mobility, recombination and extraction

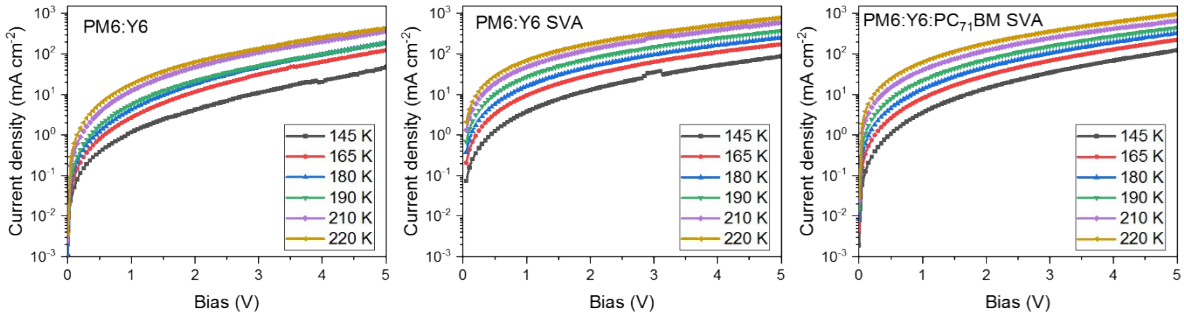

Figure S13. J–V characteristics of electron-only devices of (a) PM6:Y6, (b) PM6:Y6 SVA, and (c) PM6:Y6:$PC_{71}BM$ SVA measured at various temperature.

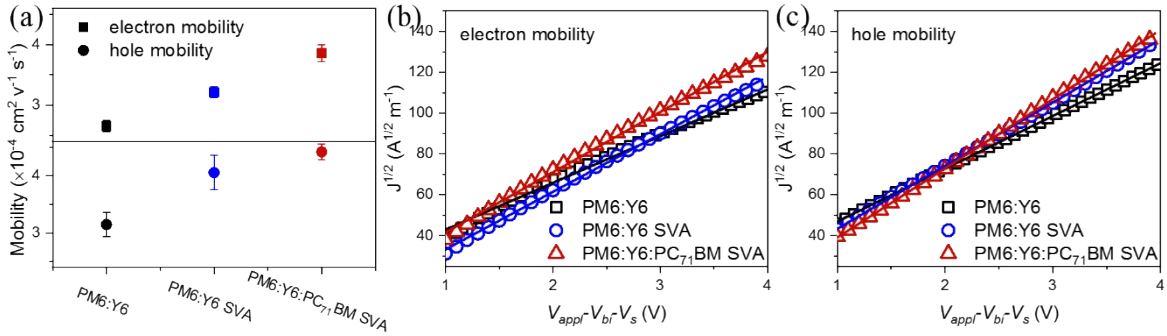

Figure S14. Carrier mobility of relating hole-only and electron-only devices.

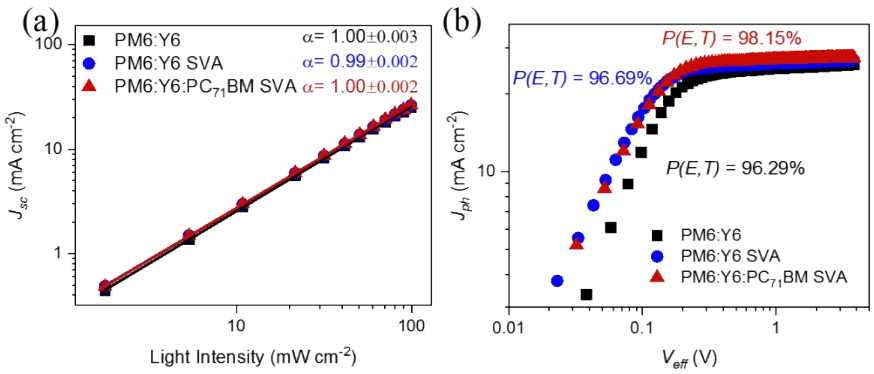

Figure S15. (a) J_{sc} plotted against light intensity and (b) photocurrent density (J_{ph}) versus effective bias (V_{eff}) of PM6:Y6-based devices.

Figure S15a shows that the relations of J_{sc} and light intensity follows the $J_{sc} \propto P_{light}^{\alpha}$ model and the values of α are almost equal to 1 for the three devices. Generally a sub-linear dependence of the photocurrent on light intensity is indicative of bimolecular recombination. A linear

dependence may result from no bimolecular recombination. Therefore, Figure S15a suggests the similar and negligible bimolecular recombination rate.

Meanwhile, the non-geminate recombination represents that free holes and electrons encounter each other once more after dissociation and recombine back to the ground state, which can be observed as three fundamentally different mechanisms: bimolecular, SRH trap-assisted, and auger. Due to the requirement for auger recombination is a high charge density, generally not believed to be present in OSCs.[8] Considering that the reduced ideality factor from the V_{oc} VS P_{light} plot (Figure 4f) suggests reduced SRH recombination in PM6:Y6:$PC_{71}BM$ SVA device. Therefore, we are able to deduce that "the PM6:Y6:$PC_{71}BM$ SVA device exhibits less non-geminate recombination than the two counterparts" in the main text.

8. Carrier dynamic

8.1 TA spectra of PM6:Y6 based blends

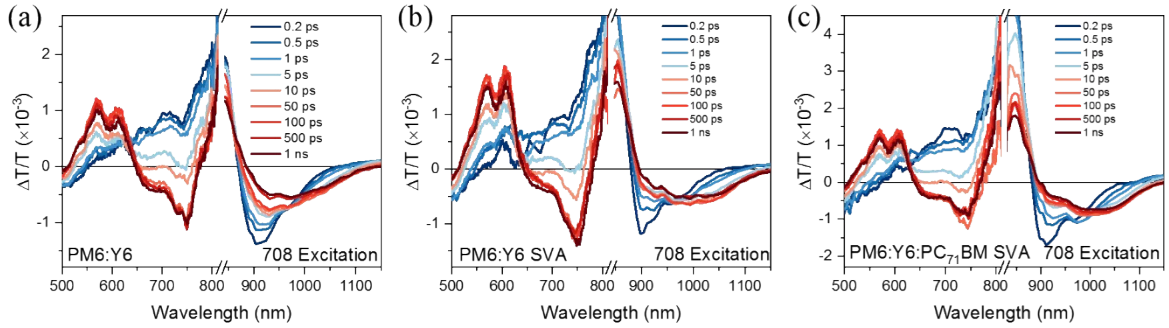

Figure S16. (a-c) TA spectra of PM6:Y6, PM6:Y6 SVA, and PM6:Y6:$PC_{71}BM$ SVA blends excited at 708 nm. The positive photo modulation signal in 550-650 nm and 800-860 nm are assigned to PM6 and Y6 ground-state bleaching (GSB), respectively. The negative and broad feature in 900-1150 nm is caused by photo-induced absorption (PIA) of exctions and charged species.

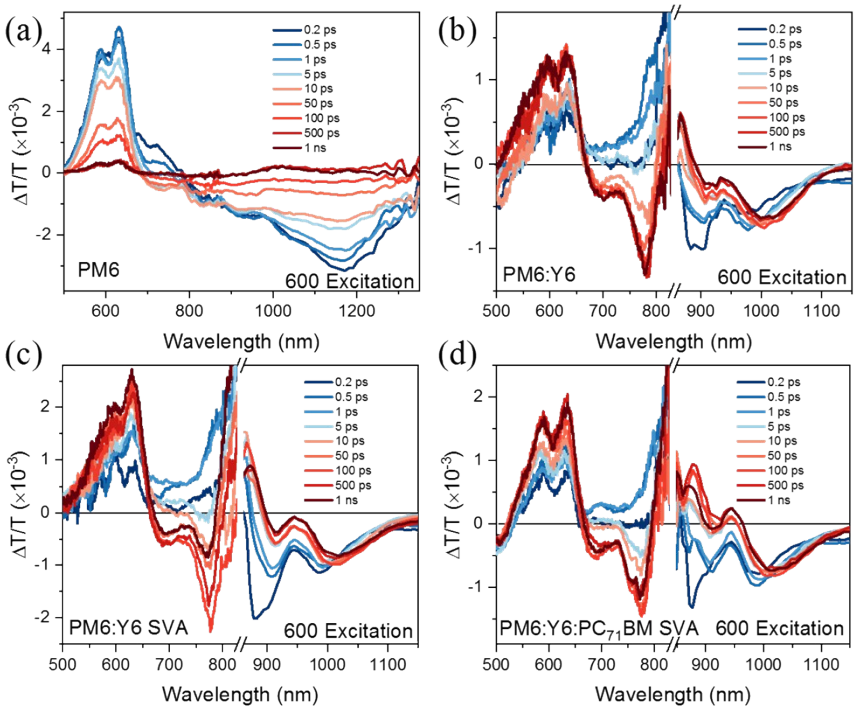

Figure S17. (a-d) TA spectra of PM6, PM6:Y6, PM6:Y6 SVA, and PM6:Y6:$PC_{71}BM$ SVA samples excited at 600 nm.

8.2 Förest energy transfer radius calculation

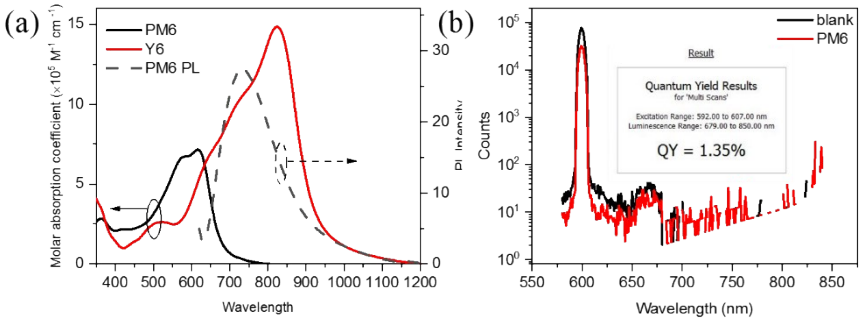

Figure S18. The molar absorption coefficient and PL intensity of PM6, Y6 neat film. (b) The quantum yield efficiency result of PM6 excited at 600 nm.

References

1. A. J. Barker, K. Chen and J. M. Hodgkiss, *J. Am. Chem. Soc.*, 2014, **136**, 12018-12026.
2. J. K. Gallaher, S. K. K. Prasad, M. A. Uddin, T. Kim, J. Y. Kim, H. Y. Woo and J. M. Hodgkiss, *Energy Environ. Sci.*, 2015, **8**, 2713-2724.

3. A. Hexemer, W. Bras, J. Glossinger, E. Schaible, E. Gann, R. Kirian, A. MacDowell, M. Church, B. Rude and H. Padmore, *J. Phys.: Conf. Ser.*, 2010, **247**, 012007.
4. E. Gann, A. T. Young, B. A. Collins, H. Yan, J. Nasiatka, H. A. Padmore, H. Ade, A. Hexemer and C. Wang, *Rev. Sci. Instrum.*, 2012, **83**, 045110.
5. A. Wagenpfahl, D. Rauh, M. Binder, C. Deibel and V. Dyakonov, *Phys. Rev. B*, 2010, **82**, 115306.
6. J. A. Bartelt, D. Lam, T. M. Burke, S. M. Sweetnam and M. D. McGehee, *Adv. Energy Mater.*, 2015, **5**, 1500577.
7. G. Zhang, X. K. Chen, J. Xiao, P. C. Y. Chow, M. Ren, G. Kupgan, X. Jiao, C. C. S. Chan, X. Du, R. Xia, Z. Chen, J. Yuan, Y. Zhang, S. Zhang, Y. Liu, Y. Zou, H. Yan, K. S. Wong, V. Coropceanu, N. Li, C. J. Brabec, J. L. Bredas, H. L. Yip and Y. Cao, *Nat. Commun.*, 2020, **11**, 3943.
8. C. M. Proctor, M. Kuik and T. Q. Nguyen, *Prog. Polym. Sci.*, 2013, **38**, 1941-1960.